Doppler sodar and radar wind profiler observations of gravity wave associated with a gravity current

F.M. Ralph, Christine Mazaudier, M. Crochet, S.V. Venkateswaran

Doppler Sodar and Radar Wind-Profiler Observations of Gravity-Wave Activity Associated with a Gravity Current

F. M. RALPH

Department of Atmospheric Sciences, University of California at Los Angeles, Los Angeles, California;

C. MAZAUDIER

Centre de Recherches en Physique de l'Environnement Terrestre et Planetaire, Saint-Maur-des-Fosses, France;

M. CROCHET

Laboratoire de Sondages Electromagnetiques de l'Environnement Terrestre, Universite' de Toulon, La Garde, France

S. V. VENKATESWARAN

Department of Atmospheric Sciences, University of California at Los Angeles, Los Angeles, California;

(Manuscript received 4 October 1991, in final form 11 June 1992)

ABSTRACT

Observations from two Doppler sodars and a radar wind profiler have been used in conjunction with data from a rawinsonde station and a mesoscale surface observation network to conduct a case study of a gravity current entering into an environment containing a nocturnal inversion and an elevated neutral layer. On the basis of synoptic and mesoscale analyses, it is concluded that the gravity current might have originated either as a scale-contracted cold front or as a gust front resulting from thunderstorm outflows observed very near the leading edge of a cold front. Despite this ambiguity, the detailed vertical structure of the gravity current itself is well resolved from the data. Moreover, the vertical velocity measurements provided by the sodars and the radar wind profiler at high time resolution have given unique information about the height structure of gravity waves excited by the gravity current. Although only wave periods, and not phase speeds or wavelengths, are directly measured, it is possible to make reasonable inferences about wave excitation mechanisms and about the influence and control of ambient stratification on wave-field characteristics. Both Kelvin–Helmholtz waves generated in the regions of high wind shear found in association with the gravity current and lee-type waves forced by the gravity current acting as an obstacle to opposing prefrontal flow are identified. It is also found that the propagation speed of the gravity current and the relative depths of the prefrontal inversion and the postfrontal cold air were not favorable for the formation of either internal bores or solitary waves at the time of day at which the gravity current was being observed.

1. Introduction

During the Mesogers field experiment in southwestern France (Weill et al. 1988), the observational network recorded the passage of an atmospheric discontinuity that was marked by a distinct and abrupt shift in wind direction, large vertical velocities, and a sharp drop in temperature. We identify this discontinuity as a gravity current and discuss the structure and plausible excitation mechanisms of the gravity waves found in association with this current. The wave characteristics are deduced from the detailed analysis of data recorded by an instrument complex consisting of Doppler sodars, a clear-air Doppler radar (henceforth referred to as the wind profiler), and a mesoscale station network that included a rawinsonde station located near the sodar and radar sites.

Atmospheric gravity currents are known to originate in various ways; for example, as sea-breeze fronts (Simpson et al. 1977), as outflows from one or several thunderstorms (Wakimoto 1982), as cold fronts that have undergone a scale-contraction process (Shapiro et al. 1985), or as a dryline (Parsons et al. 1991).

Fulton et al. (1990), Doviak et al. (1991), and Koch et al. (1991) have studied gravity currents generated by thunderstorm outflows and have observed bores and/or solitary waves triggered by such events. Mueller and Carbone (1987) and Weckwerth and Wakimoto (1991) have identified Kelvin–Helmholtz (KH) waves atop the cold air associated with gust fronts.

The contraction of a cold front into a gravity current may result from precipitation processes (Carbone 1982; Seitter and Muench 1985) but is also found to occur in the absence of precipitation (Shapiro 1984; Young

Corresponding author address: Dr. F. Martin Ralph, NOAA/ERL Wave Propagation Laboratory, 325 Broadway, Boulder, CO 80303-3328.

and Johnson 1984; Shapiro et al. 1985). In the latter case, satellite imagery often shows a well-defined rope cloud even though there is no nearby deep convection. Such clouds have been observed within the narrow band of strong upward motion at the leading edge of cold fronts (Shapiro et al. 1985).

Based on the data available to us on the relevant scales of motion (sections 3 and 4), it is apparent that the gravity current may have marked the passage of either a scale-contracted cold front or a gust front created by thunderstorm outflows. Strong convective precipitation had occurred on the colder side of the gravity current but had ceased 1–2 h before the gravity current actually passed the center of the experimental network. Examination of DMSP (Defense Meteorological Satellite Program) and GOES (Geostationary Operational Environmental Satellite) satellite imagery on 27 and 28 September (not shown) revealed the cold front as a broad eastward-moving cloud bank roughly 300 km across and 2000 km long with embedded areas of deep convection. The leading edge of this broad, cold-frontal cloud band was marked by high clouds that reached the experimental area at nearly the same time as the gravity current and that could have obscured the satellite view of any rope cloud that was present. Although the available data were unable to resolve the exact placement of the gravity-current discontinuity within the deeper baroclinic system, the proximity of the gravity current to the leading edge of the larger-scale baroclinic zone would suggest that we might have encountered a case of frontal scale contraction resembling that proposed by Seitter and Muench (1985). Our case then falls between the well-documented cases of frontal contraction developing with or without precipitation processes actively modifying the front.

The ambiguity in our data regarding the mode of origin of the gravity current is believed to have no immediate bearing on the principal objective of this paper, which is to arrive at a collated and coherent picture of gravity waves excited and maintained in the ambient environment close to the gravity current. The emphasis is on the vertical structure of the waves, on the influence of the ambient environment on wave activity, and on the potential wave-forcing mechanisms. Numerous previous studies involving field and laboratory experiments or numerical models have provided valuable clues regarding the types and properties of wave behavior (Clark et al. 1986; Mueller and Carbone 1987; Simpson 1987; Kuettner et al. 1987; Droegemeier and Wilhelmson 1987; Crook 1988; Haase and Smith 1989; Carbone et al. 1990; Cheung and Little 1990; Nastrom et al. 1990; Doviak et al. 1991; Haase 1991; Koch et al. 1991).

2. The data

The Mesogers field experiment, performed in southwestern France in September and October 1984 (Weill et al. 1988) was specifically designed to provide test data for parameterization schemes to be adopted in mesoscale numerical forecast models. As shown in Fig. 1, an array of instruments was distributed mostly in a 50-km × 50-km square (to be referred to as the Mesogers area). This array consisted of a surface observation network [the PATAC (Prévision Améliorée Technique d'Affinements de la Climatologie) network] measuring wind, temperature, and humidity at half-hour intervals and precipitation at 6-min intervals; a rawinsonde station that conducted special ascents for the experiment; and remote-sensing instruments consisting of a vertically pointing radar wind profiler and several sodars of various types.

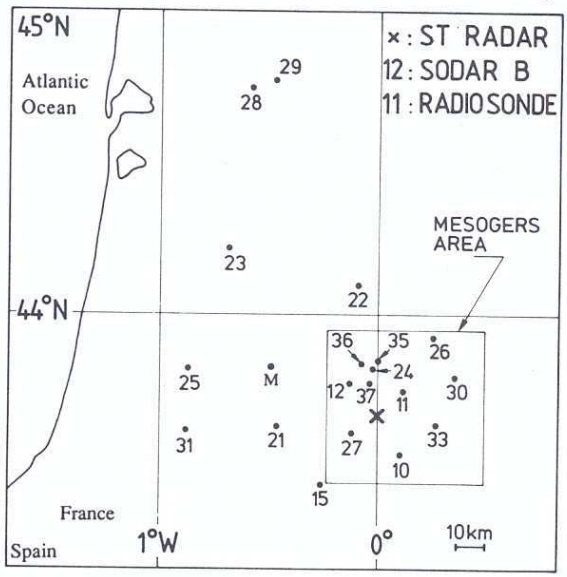

FIG. 1. Basemap for the Mesogers experiment located in southwestern France. Numbered dots show the locations of instruments that were part of the PATAC mesonetwork of surface stations. Special rawinsonde ascents were made from station 11. Additional instruments used in this study are the 45-MHz wind profiler (marked ×) and two 2000-Hz Doppler sodars (A at station 35, and B at station 12).

The 45-MHz radar wind profiler measured vertical velocities at roughly 2-min intervals from 1.2 to 10 km AGL (above ground level), with 300-m vertical resolution [see Gage (1990) for a review of wind-profiler techniques].

A 2-kHz Doppler sodar (sodar B), separated 12 km from the wind profiler, measured horizontal and vertical velocities at 4-s and 12-s intervals, respectively, from 19 to 476 m AGL, with 15-m height resolution. There were other sodars operating farther from the wind-profiler location and making additional wind measurements. This combination of in situ and remote-sensing instruments was able to monitor surface atmospheric wind discontinuities, their lower tropospheric extensions, and their effects on the free tro-

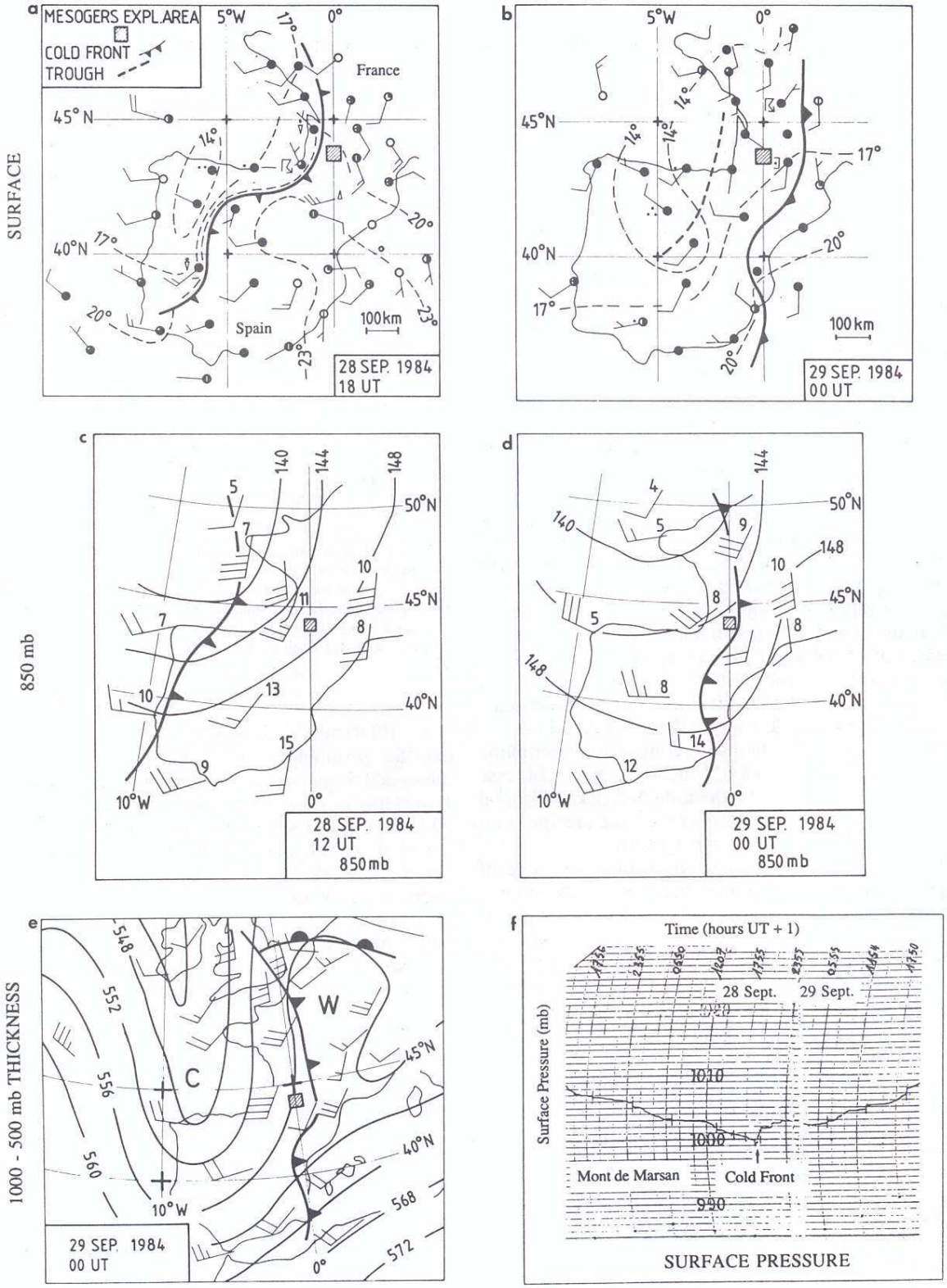

FIG. 2. Synoptic conditions associated with the surface cold front. The central Mesogers experimental area is shown as a hatched box. (a) Surface analysis at 1800 UTC 28 September 1984, 1 h prior to frontal passage at the wind profiler, is shown with isotherms (°C, dashed lines), winds (full barb is 5 m s^{-1}), weather, cloudiness, and frontal position. (b) Same as in (a) but at 0000 UTC 29 September (5 h after frontal passage at the wind profiler). The 850-mb charts with winds, temperatures (°C), geopotential heights (dam, thin solid lines), and frontal positions are shown for (c) 1200 UTC 28 September and (d) 0000 UTC 29 September. (e) The 1000–500-mb thickness chart (dam) with 700-mb winds and surface frontal positions are shown. Regions of cold air (C) and warm air (W) are marked. Notice the location of the synoptic-scale trough. (f) Pressure trace from Mont de

posphere well above the surface. It should be noted that the 6.67-m wavelength of the radar wind profiler is sufficiently long that the effect of hydrometeors on the observed wind is relatively small.

3. The synoptic-scale perspective

The synoptic-scale conditions are shown in Fig. 2. The surface analysis of standard weather data at 1800 UTC 28 September (Fig. 2a) shows the appearance of a cold front, about 50 km inland from the coast near 45°N and about 50 km west of the Mesogers area. Ahead of the front both in southwestern France and in Spain the flow was primarily southerly or easterly, while west of the front the flow had more of a westerly and northerly component. A few stations dominated by terrain effects show departures from this prevalent pattern. The temperature contrast across the front was approximately 6°C over western Spain, but only approximately 3°C over France. The front was marked by a broad band of cloudiness and scattered precipitation, including showers and thunderstorms west of the Mesagers area, although within the area itself (e.g., at the profiler and sodar sites) no precipitation was observed in direct association with the frontal passage.

During the six hours following 1800 UTC 28 September, the front had propagated to the east of the Mesogers area (Fig. 2b). The signature of the front is seen at 850 mb (Figs. 2c and 2d) as a shift to more westerly flow, moving across most of Spain between 1200 UTC and 0000 UTC and entering western France (and crossing the Mesogers area) by 0000 UTC 29 September. Ahead of the front the flow was southerly and there was some indication of a low-level jet.

While the 850-mb temperatures ahead of the front did not change from 1200 to 0000 UTC 29 September, there was a temperature drop of 3°–5°C during this time interval at stations across which the front had passed.

The 1000–500-mb thickness pattern (Fig. 2e) shows that the frontal boundary was close to the leading edge of a synoptic-scale pool of cold air and ahead of a large-scale trough. The trough axis was located to the west of the Mesogers area at 0000 UTC 29 September. The thickness pattern further indicates that the cold air was deeper and/or colder near the trough axis than behind the leading edge of the front, as is typically observed for a cold front.

The surface frontal passage was marked by a distinct pressure minimum in the barograph trace (Fig. 2f) from Mont de Marsan (labeled M in Fig. 1). Subsequent to the frontal passage, the wind directions recorded by the Mesogers network remained steady for several hours.

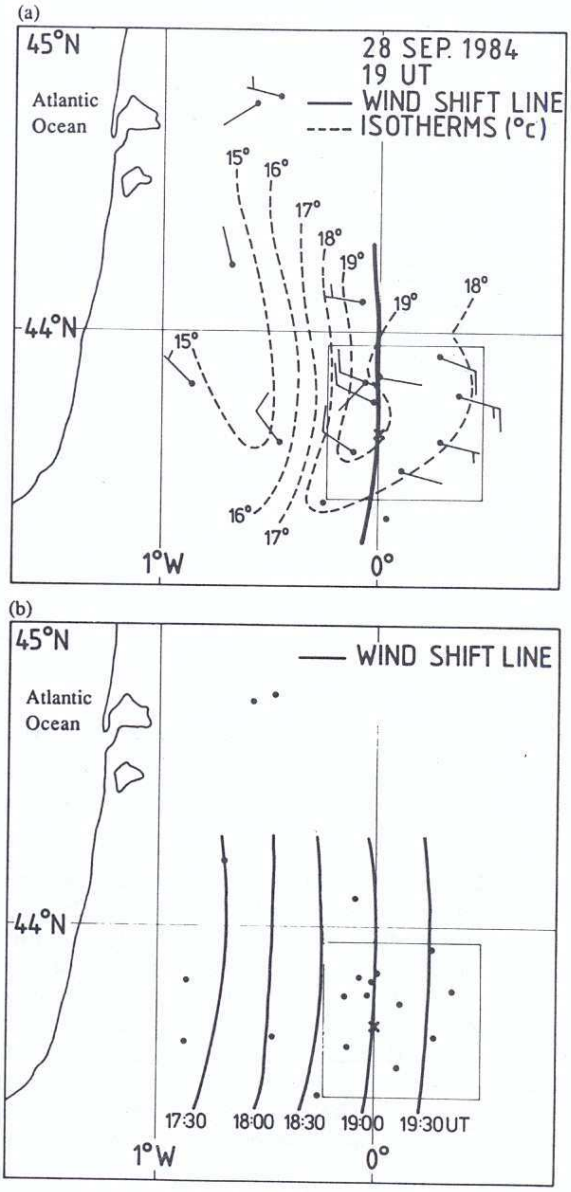

FIG. 3. Mesoscale frontal analyses based on observations from the PATAC network (dots) and from the sodars. The Mesogers area is shown as a box (50 km on a side). Frontal positions, defined by the wind-direction shift, are shown as bold solid lines. (a) Surface mesoanalysis for the time of frontal passage at the radar wind profiler (labeled ×), with temperatures in degrees Celsius and winds as in Fig. 2. (b) Isochrones of frontal position at 30-min intervals, yielding the 10 m s^{-1} frontal speed.

4. Meso- and microscale frontal characteristics

We now examine the mesoscale (~100 km) and microscale (~100 m) behavior of the front, using the scale terminology recommended by Orlanski (1975).

Marsan (labeled "M" in Fig. 1) showing the frontal trough and the 2–3-mb pressure jump. Although the coordinate system and station locations are clearly marked in each of the panels (a)–(e), it should be noted that there are differences in projection, scale, and coastal outlines from one panel to another.

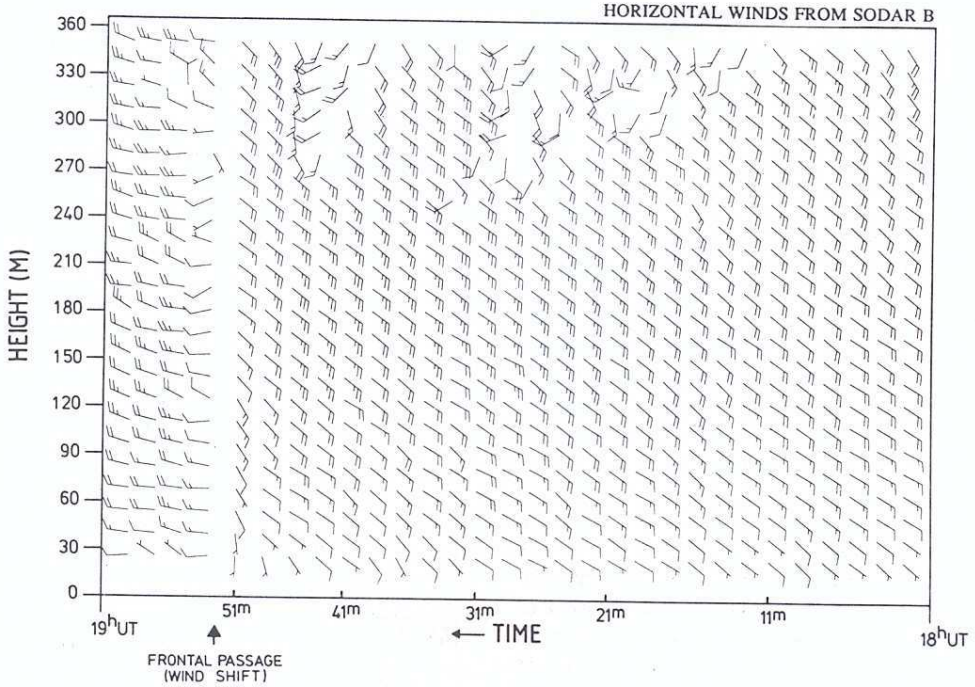

FIG. 4. Two-minute averages of the horizontal winds measured by sodar B from 1800 to 1900 UTC 28 September 1984. Full barb is 5 m s^{-1}. Time runs from right to left. The front is marked by an arrow. The data points ahead of the front and above 250 m, which might appear to suggest that some wave activity was present, are judged to be unreliable owing to the weakness of the recorded signal.

Figure 3a shows that the front was marked by a shift of wind direction from easterly flow ahead of the front to northwesterly flow behind it, and by temperature drops of 3°–4°C. The appearance of the warmest air somewhat behind the wind-shift line in this figure is the likely result of differences in the adopted averaging times for the wind (the last 10 min of each half-hour) and temperature (the entire half-hour) observations. According to Fig. 3b, the front had a propagation speed of 10 m s^{-1} from the west when it reached the Mesogers area by 1830 UTC 28 September 1984. The frontal passage was observed by sodar B inside this area as a horizontal wind shift of almost 180° occurring within the lowest 360 m in less than 2 min (Figs. 4 and 5), a feature also repeated at the other sodars (not shown). Although such a wind shift by itself might signal either a gust-front passage or the passage of a collapsed cold front, recall that the wind discontinuity occurred near the leading edge of a synoptic-scale pool of cold air forming part of an extensive baroclinic zone. Furthermore, the pressure trace in Fig. 2f shows that the lowest recorded pressure coincides almost exactly in timing

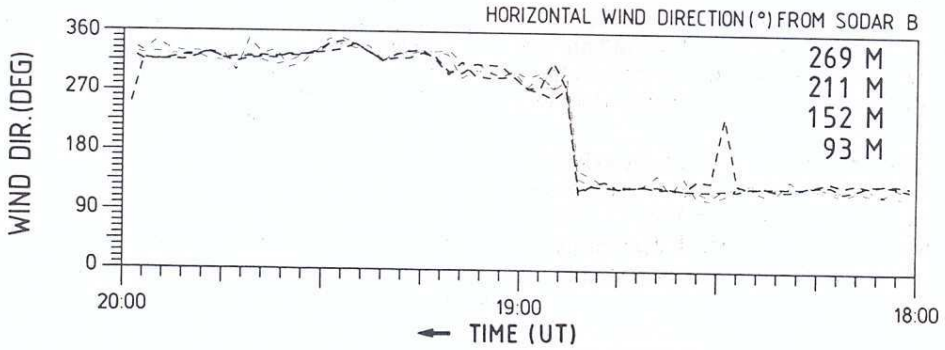

FIG. 5. Time series of horizontal wind direction at selected heights from sodar B showing the distinct wind shift that marks the frontal passage, and the steadiness of the wind direction ahead of and behind the front. The one odd point at approximately 1830 UTC is at 269 m and corresponds to the anomalous data points seen above 250 m and ahead of the front in Fig. 4.

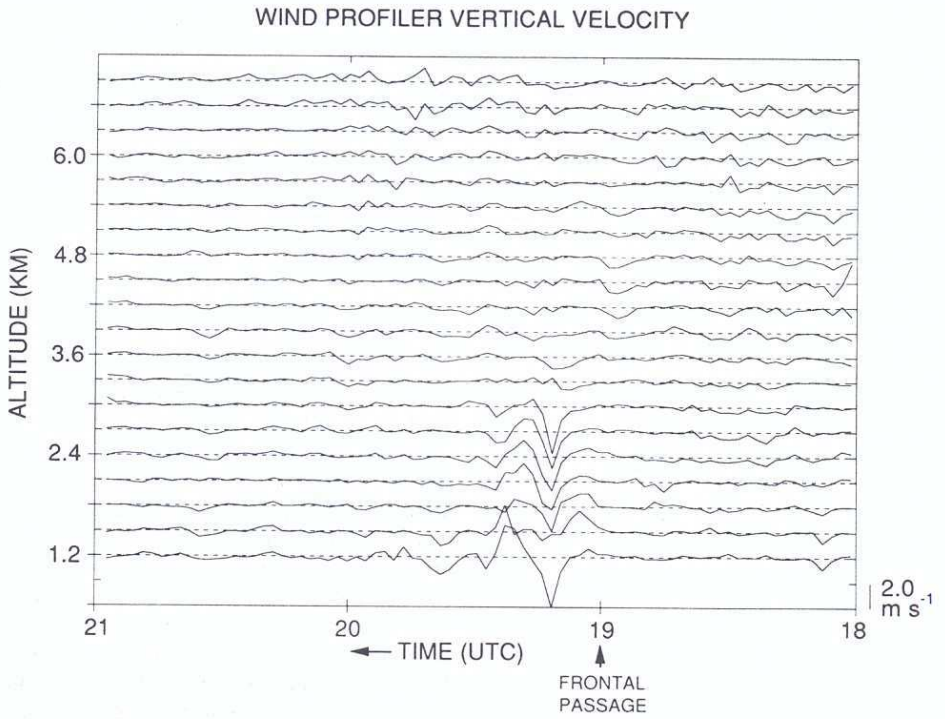

FIG. 6. Time–height cross section of vertical velocities observed by the 45-MHz radar wind profiler. Vertical velocities were measured continuously and represent roughly 2-min averages. As in Figs. 4 and 5, time is reversed. The time of frontal passage at the wind profiler site is also marked.

with the frontal passage. This coincidence is quite characteristic of cold fronts. At the same time, the abruptness and magnitude of the pressure jump (2–3 mb) would suggest that the cold front had by then scale contracted into a gravity current. Possible contributions to this gravity current from thunderstorms occurring to the west of the Mesogers area will be discussed later in this section.

Vertical velocity observations from the wind profiler (Fig. 6), as well as temperature and moisture soundings from the nearby rawinsonde station (Fig. 7), have helped portray the atmospheric conditions before and after the frontal passage at heights not accessible to the sodars (i.e., above 476 m AGL). The rawinsonde launched at 1923 UTC 28 September, a few minutes after surface frontal passage, shows that the air immediately behind the front was 4°C cooler than the prefrontal air, reaching a depth of 1.4 km within a few minutes after frontal passage, as would be symptomatic of either a gust front or a gravity current. The prefrontal thermal conditions could be determined only from a temperature sounding that was launched 5 h before the frontal passage (1400 UTC), although the sounding at 1850 UTC (Fig. 8) gave the winds just ahead of the front.

A cross section of the gravity-current boundary and its immediate environment, as constructed from the sodar, wind-profiler, and rawinsonde data is shown in Fig. 9. In arriving at this cross section, the data from these instruments are centered on the time of passage of the boundary at their respective sites. Notice, however, that the wind profiler and the nearest sodar are 12 km apart and that there is an 800-m vertical gap between the highest level for which the sodar data and the lowest level for which the wind profiler data are available.

Figure 9 succeeds in demonstrating the sharpness of the gravity-current boundary and the strong vertical velocity disturbances clearly related to the gravity current. The disturbances are semiperiodic in nature, have amplitudes in excess of 1 m s^{-1}, and last for nearly an hour. These features are discussed further in section 5.

In order to evaluate the effects of frontal lifting, we have constructed a hypothetical prefrontal rawinsonde sounding for approximately 1900 UTC from the available sounding at 1400 UTC (Fig. 7a) and from such additional information as is available. Thus, we make use of the observed prefrontal surface temperature and dewpoint at 1900 UTC (19° and 14°C, respectively), the observed diurnal maximum surface temperature in the area (27°C), and the depth of the surface cool layer (250 m). The depth of the surface inversion is estimated to be the same as that of the high-reflectivity layer in the sodar facsimile chart (Fig. 10), based on the observed high correlation between the decreasing surface temperatures (due to radiational cooling) and the increasing depth of the high reflectivity layer, during the hours before frontal passage. We modify the 1400 UTC sounding by first raising the surface temperature from 25° to 27°C. This gives a mixed-layer depth of

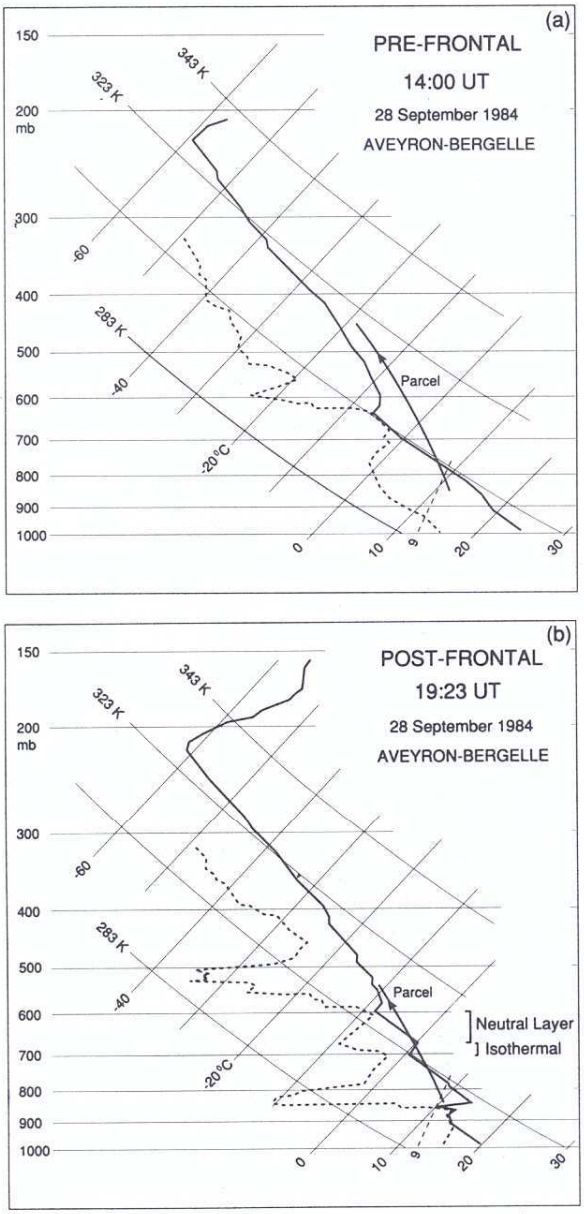

FIG. 7. Rawinsonde observations from station 11 at (a) 1400 UTC and (b) 1923 UTC. Temperature (solid) and dewpoint temperature (dashed) are shown. The wet-bulb temperature of a parcel lifted from the surface (after mixing the lowest 50 mb) is shown for each sounding. The 9 g kg^{-1} mixing ratio line is shown for reference. The 1923 UTC sounding was launched less than 10 min after frontal passage. The elevated neutral layer and the adjacent isothermal layer discussed in the text are also identified in (b).

about 1.2 km. We next lower the surface temperatures to 19°C and assume a linear temperature increase with height from the surface to the preexisting temperature at 250 m AGL. This procedure yields the hypothetical prefrontal sounding for 1900 UTC that is shown in Fig. 11.

Comparison of the pre- and postfrontal soundings at 1900 and 1923 UTC, respectively, shows that 1) the layer AA' in the prefrontal sounding has been lifted by about 140 mb to become the layer BB' in the postfrontal sounding [This type of lifting has been observed by Mueller and Carbone (1987) and has been simulated in the numerical model of Droegemeier and Wilhelmson (1987)]; 2) the surface layer in the prefrontal sounding has been lifted to 860 mb, with condensation occurring at the anticipated lifting condensation level (LCL); 3) the vertical extent of updrafts is limited by the isothermal layer below 700 mb, behavior which is in accord with the wind-profiler vertical velocity observations (Fig. 6); and 4) the effects of the frontal passage on the soundings are limited to below 600 mb, with no observed changes above this level between 1400 and 1923 UTC.

Some additional comments on the postfrontal sounding at 1923 UTC are in order. It would appear that this sounding was launched very close to the frontal boundary since frontal passage occurred at the launch site sometime between 1910 and 1920 UTC. In addition, the recorded moisture and temperature profiles at low levels seem to indicate that the balloon was in an updraft. The subsidence layer in this sounding, between 620 and 700 mb, and the extremely dry air, between 850 and 780 mb, cannot be accounted for in terms of the data available for this study. Similarly, the fate of the prefrontal air between 840 and 700 mb in the region ahead of the front also remains unclear.

The preceding analysis of the frontal effects serves to highlight the fact that, although air parcels forced

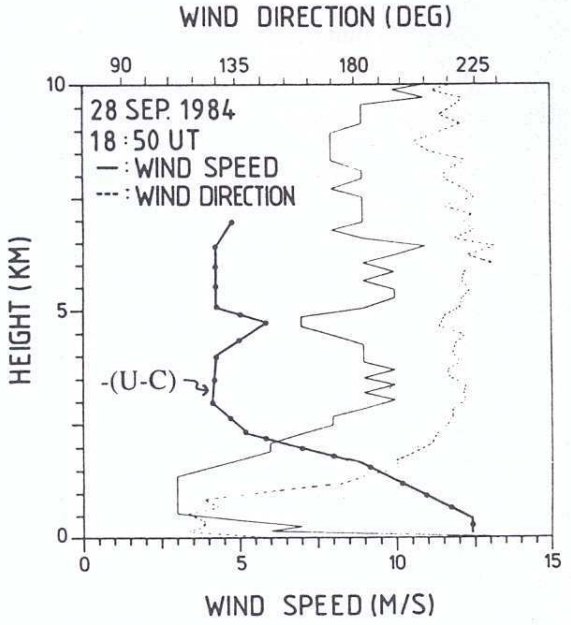

FIG. 8. Wind profile observed by rawinsonde from station 11 at 1850 UTC, just prior to frontal passage. Note that temperature and moisture information were not available from this sounding. The front-relative flow ($u - c$), where c is the frontal speed of 10 m s^{-1} from the west and u is the flow parallel to frontal motion, is also shown.

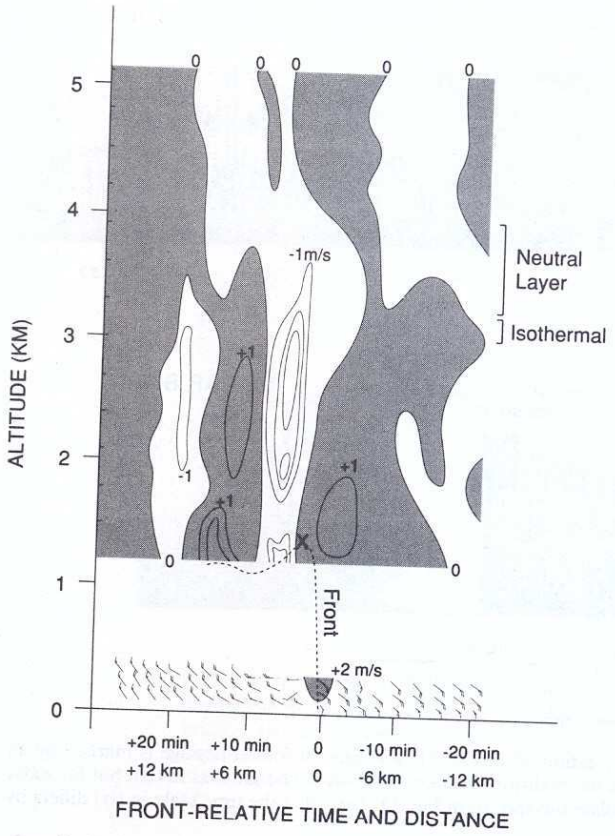

FIG. 9. Synthesis of profiler, sodar, and rawinsonde observations of the gravity current. Vertical cross section showing sodar-observed vertical velocities up to 0.35 km and radar-observed vertical velocities above 1.2 km (contoured at 1 m s^{-1} intervals, shading represents upward motion), 2-min-averaged horizontal winds observed by sodar B below 360 m (plotted with same wind barb notation as in Fig. 2), and the inferred structure of the frontal boundary (the rawinsonde-observed depth of the cold air is shown as an ×). Note that the times shown are with reference to the time of frontal passage and that a time–space conversion using C_{front} = 10 m s^{-1} is adopted on the x axis. The rawinsonde-observed neutral and isothermal layers are also marked.

upward by the front may have reached the level of free convection (LFC) at approximately 750 mb (Fig. 7a), the isothermal layer from 680 to 700 mb that had appeared before 1923 UTC sounding would have set an upper limit to the altitude up to which such air parcels could have risen. Hence, it seems reasonable to conclude that forcing of deep convection by the front was inhibited in the Mesogers area. This is in agreement with the observation that no precipitation was recorded as the front crossed this area.

Although no rain was recorded during frontal passage at the sodar (Fig. 12f) or at the radar site (based on the radar logbook), precipitation had occurred when the front had passed stations to the west of these sites at earlier times (Figs. 12a–d). The rainfall rate at some of these stations had exceeded 100 mm h^{-1} for 6-min intervals, yielding up to 42 mm in 1 h and indicating that intense convective activity was present west of the Mesogers area. The evidence for deep convection is also present in the surface synoptic charts (Figs. 2a and 2b), which show that thunderstorms occurred behind the front. The diabatic cooling due to hydrometeors associated with such convective precipitation could have added to the synoptic-scale differential cold advection and intensified the cold front, thereby transforming it to take on the characteristics of a gravity current, in the manner earlier proposed by Carbone (1982). Although an example of such diabatic forcing is shown in Carbone (1982), which also had rainfall rates on the order of 100 mm h^{-1}, its role in the scale contraction of the cold front has not yet been quantified. Unlike Carbone (1982) in which a squall line was essentially collocated with the cold front, Seitter and Muench (1985) proposed a scenario in which a gust front originates from strong precipitation behind the cold front but moves out ahead of the cold front. In these cases, as well as in ours, the distinction between a gust front and a cold front becomes less well defined.

The decrease in frontal precipitation observed in our case as the front propagated eastward might have occurred partly as a result of radiational cooling that had reduced the surface temperatures. This is evident from Fig. 7b, which indicates that if prefrontal surface temperatures had been 1°–2°C higher than at the time of frontal passage, it is likely that strong enough updrafts would have been able to penetrate the isothermal layer near 3 km and reach heights of up to 8 km. Thus, it would appear that the development or decay of frontal convective precipitation could have been modulated by the diurnal cycle and, in turn, modify the frontal characteristics on a diurnal basis from the attendant cycle in evaporative cooling (and possibly melting) processes. This type of diurnal modulation of the front can become evident when the frontal forcing by itself is barely able to initiate convective instability in an otherwise marginally stable environment. Our limited dataset is at best suggestive of this diurnal association between convection and the structure of fronts.

While the sodar data give a detailed picture of the wind field associated with the front below 500 m, the radar wind-profiler observations (Figs. 6 and 9) show that the frontal passage was marked by vertical velocities of up to 3 m s^{-1} above 1.2 km. Such vertical velocity values are typical of frontal situations at these altitudes, as reported from observations using either aircraft (Shapiro et al. 1985), 3–10-cm Doppler radar (Wakimoto 1982; Mueller and Carbone 1987; Mahoney 1988; Hoinka et al. 1990), or Doppler lidar (Parsons et al. 1991). As in the gust front studied by Mueller and Carbone (1987), the strong vertical motion for our front was confined to altitudes below 3.5 km, and in both cases, the depth of the updraft was limited by an isothermal layer at 3–4 km AGL (Fig. 7b). Mueller and Carbone (1987) had to infer the vertical extent of their disturbances indirectly that is, from the absence of radar returns above 3.5 km. In our case, however, the deduction of the vertical extent of the

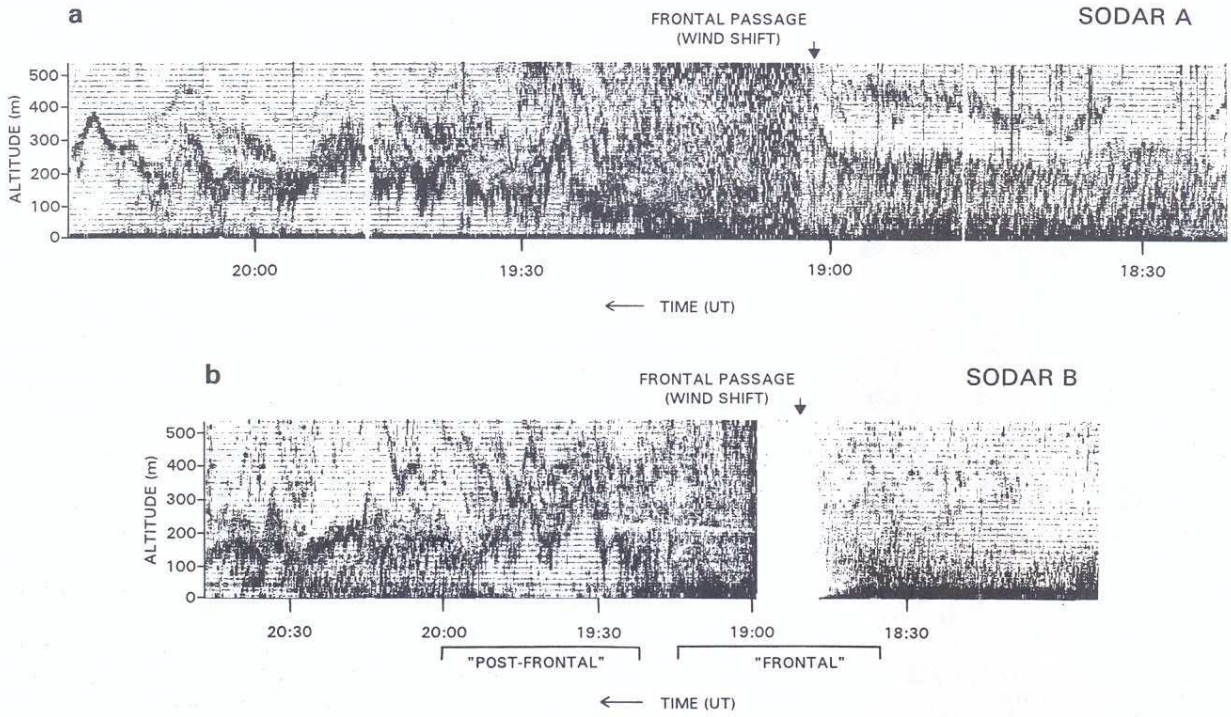

FIG. 10. (a) Facsimile record from an oblique antenna of sodar A (station 35 in Fig. 1). The time of frontal passage is marked by an arrow. Notice the high reflectivity at 250 m AGL marking the depth of the prefrontal surface stable layer. (b) Same as in (a), but for sodar B, and showing the frontal and postfrontal data intervals used to calculate the spectra in Fig. 15. Note that the time scale in (b) differs by a factor of 2 from that in (a).

disturbances from the wind-profiler vertical velocity data is more direct.

We now proceed to show that the front, observed by the sodar and the radar wind profiler, had a propagation speed and several microscale features that serve to identify it distinctly as a gravity current.

The propagation speed V of a density or gravity current is governed by the formula (Seitter 1986)

$$V = k\left(\frac{\Delta p}{\rho}\right)^{1/2},$$

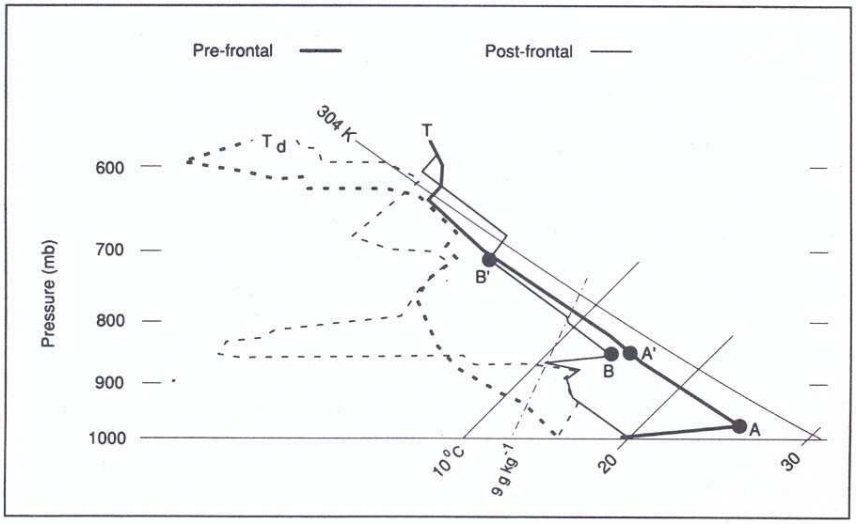

FIG. 11. Comparison of pre- and postfrontal soundings. Same notation as in Fig. 7. Layer AA' has been lifted to become layer BB'.

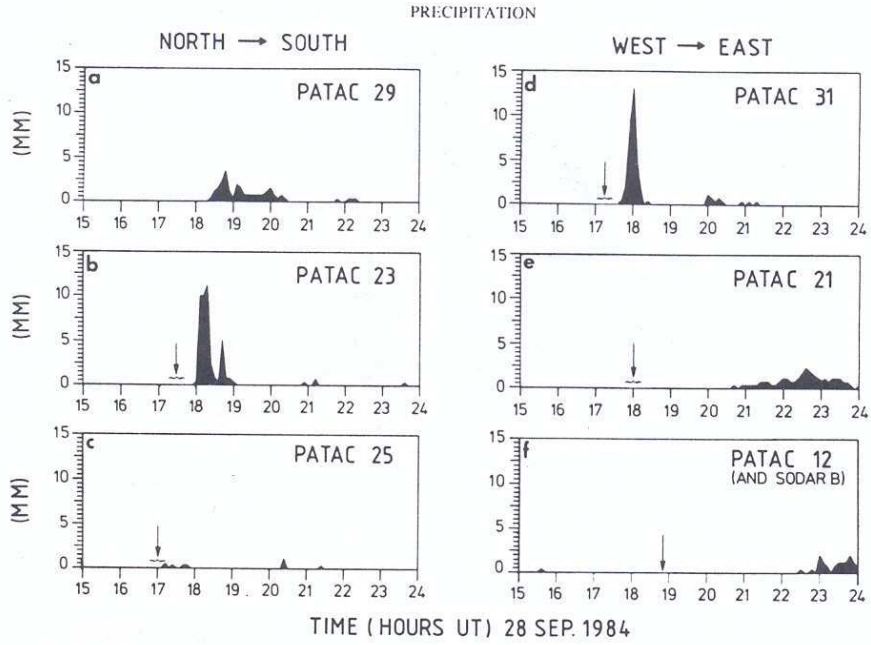

FIG. 12. Precipitation records from various PATAC stations (measured as rainfall accumulated during 6-min intervals). Time of frontal passage at each site is marked by an arrow and/or brackets that denote the interval during which frontal passage must have occurred at that station, as judged from the PATAC data with 30-min time resolution. Stations 29, 23, and 25 are all west of the central network (Fig. 1) and are on a line oriented north–south, while stations 31, 21, and 12 are on a west–east line ending at the center of the network.

where ΔP is the total difference in surface pressure between the gravity-current head and the environment, ρ is the surface density of the warm air ahead of the gravity current, and k is a constant. Use of the total pressure difference rather than the hydrostatic pressure difference and use of the density at the surface rather than the average density over the depth of the gravity-current head are approximations that introduce errors that are small relative to the uncertainty in k, which has the attribute of an internal Froude number (Seitter 1986; Smith and Reeder 1988). For our case, $\Delta p = 200$ Pa and $\rho = 1.19$ kg m^{-3} giving $V = k \times 13.0$ m s^{-1}.

Both laboratory experiments (Simpson and Britter 1980) and field observations indicate that the propagation speed relative to the ground needs to be modified by approximately three-fifths of the speed of the ambient prefrontal flow parallel to the frontal motion. If we add three-fifths of the opposing flow in the prefrontal air (obtained as an average over the lowest 1.4 km in the 1850 UTC sounding) to the observed propagation speed (10 m s^{-1}) of the front, we deduce a value of 0.9 for k that is well within the range quoted for gravity currents (Koch et al. 1991; Fulton et al. 1990).

High-resolution sodar data contain significant additional information about the structure of the gravity-current boundary. To recover this information, we have analyzed the sodar data sampled at 12-s intervals (Fig. 13), corresponding to horizontal scales of approximately 100 m rather than the approximately 1-km scale of the 2-min-averaged data of Fig. 4. These spatial scales were estimated from the 10 m s^{-1} propagation speed of the front. The front itself was identified kinematically as the zero front-normal horizontal velocity contour (Fig. 13a), as in Goff (1976). Flow of postfrontal air toward the front, resulting from front-normal wind speeds in excess of the 10 m s^{-1} translational velocity of the front, was found approximately 600 m behind the front. This flow had maximum speeds between 50 and 100 m AGL (Fig. 13a). Below 50 m, the eastward component was less than the 10 m s^{-1} eastward motion of the front itself, and thus, constituted a return flow relative to the frontal motion. Above a level of minimum winds near 200 m, there was a region of increasing front-normal flow that extended above the vertical range of the sodar. At about 200 m ahead of the front there was a jet with maximum speed normal to the front in excess of 7 m s^{-1}.

The vertical velocity pattern on the 12-s time scale (Fig. 13b) has remarkable verisimilitude with patterns found for several gust fronts from instrumented tower observations (Goff 1976). The primary features include a 1–2-km-wide updraft centered on the kinematic boundary, with vertical velocities increasing from almost zero near the surface to greater than 3 m s^{-1} at 300 m and above; a systematic pattern of up and down motion behind the front; and downward motion below the low-altitude postfrontal jet (i.e., below 100 m from 50 min 30 s to 51 min 40 s in Fig. 13b).

In addition, close inspection of the data reveals a

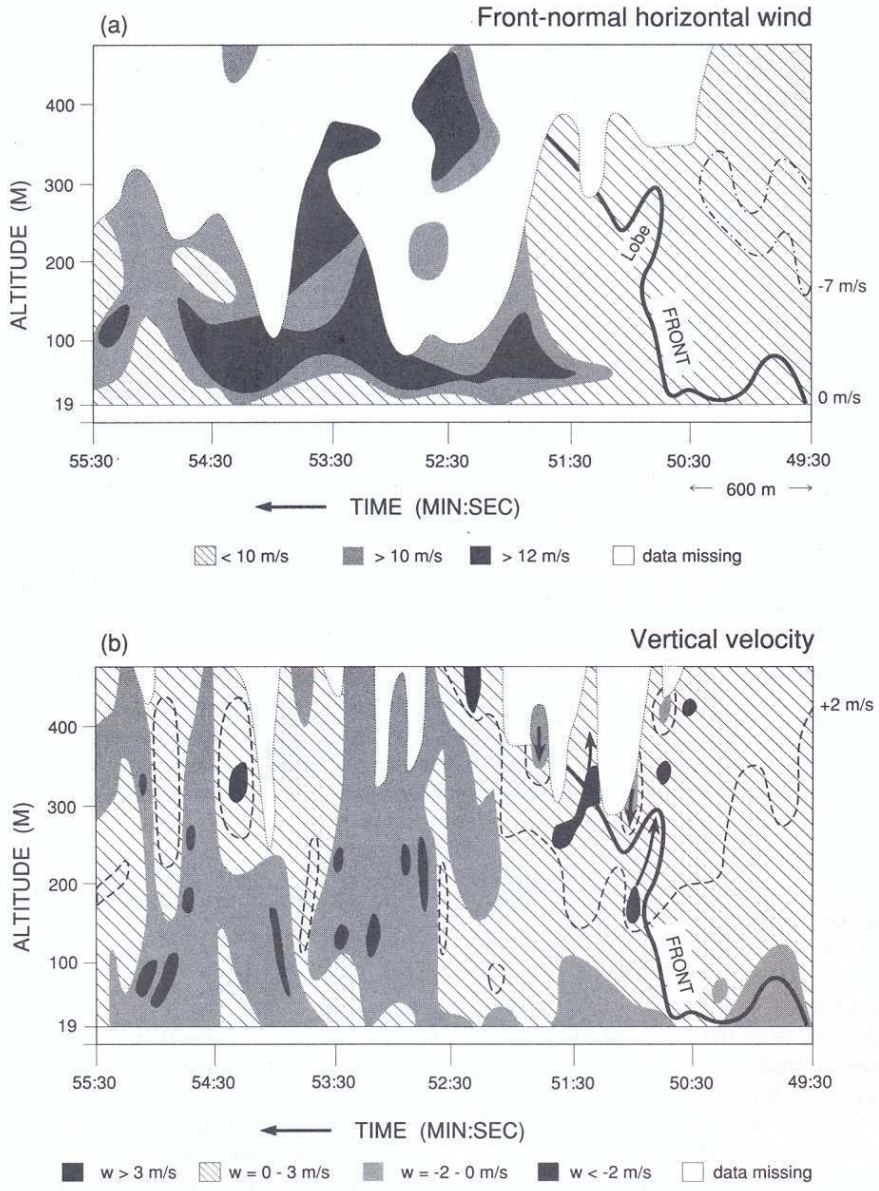

FIG. 13. (a) High time resolution sodar observations of horizontal winds normal V_N to the frontal motion C_{front}. The kinematically defined frontal boundary (i.e., $V_N = 0$) is shown as a bold line. Note the lobe of postfrontal air referred to in the text. Shaded areas represent flow with $V_N > C_{\text{front}}$ (i.e., postfrontal air moving eastward faster than the 10 m s^{-1} eastward motion of the front). Hatched areas have $V_N < C_{\text{front}}$. The contour $V_N = -7$ m s^{-1} shows the prefrontal low-altitude jet. In both (a) and (b), clear areas surrounded by dotted lines represent missing data. (b) Areas of upward motion (hatched) and downward motion (shaded) are shown. The location of the front is based on part (a) of this figure. Arrows mark couplets of downward motion and enhanced upward motion, including one associated with the lobe of postfrontal air. A horizontal distance scale based on the frontal motion is shown for reference.

lobe of westerly flow (Fig. 13a) consisting of postfrontal air protruding into prefrontal air. Coincident with this perturbation in the kinematic frontal boundary is a disturbance in the vertical velocity showing upward motion in the lobe and downward motion just behind it (Fig. 13b). A similar but less distinct vertical velocity couplet is detectable farther up along the frontal boundary. The spatial scale of these features is much less than the scale of the general frontal updraft in which they are embedded. These features are probably related to the formation of Kelvin–Helmholtz (KH) billows that can act to mix air across the front, which is sloped at about 45° in this region. There is corroborative evidence for such mixing in the postfrontal sounding (Fig. 7b), which has a highly structured layer (from 900–850 mb above the surface cold air) in which a shallow

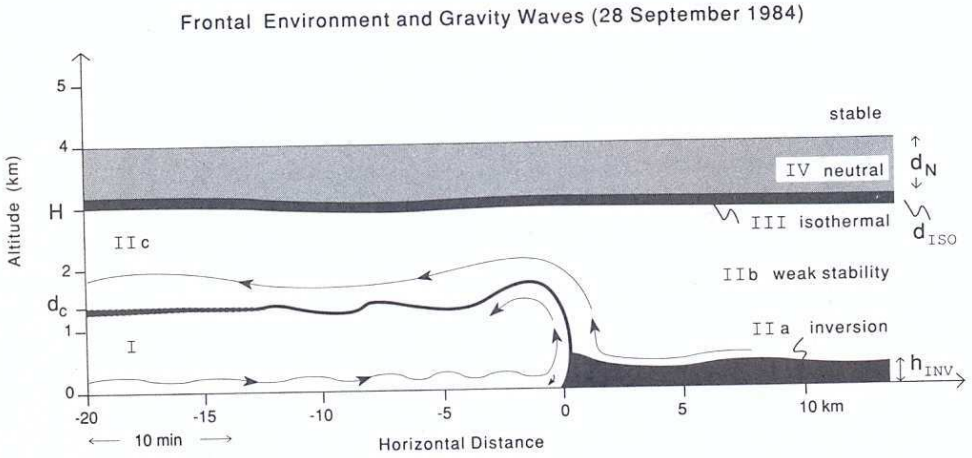

FIG. 14. Schematic of observed gravity-wave behavior associated with the gravity current, including front-relative flow and aspects of the ambient stratification that are important to wave activity and to frontal structure. Zones I, II, III, and IV are defined in the text and in Table 1. Here H is the base height of the elevated inversion (zone III), h_{INV} is the depth of the prefrontal radiation inversion, d_c is the depth of the cold air, d_N is the thickness of the elevated neutral layer, and d_{ISO} is the thickness of the elevated isothermal layer. A time scale based on frontal motion is shown for reference.

superadiabatic sublayer (between 865 and 855 mb) is embedded. Since quantitative information about the Richardson number at the top of the cold air is not available (because the 1923 UTC sounding was postfrontal and measured temperatures but not winds, while the 1850 UTC sounding was prefrontal and measured only winds), we can only guess that the vertical shear between the cold air below and the prefrontal air above the front could have induced KH instability, as has been observed elsewhere under similar circumstances.

It might be useful at this stage to recapitulate the thrust of sections 3 and 4. The atmospheric discontinuity described so far might have originated as thunderstorm outflows as is supported by the fact that deep convection and large rainfall rates were present roughly 100 km to the west of the center of the observing network until 1–2 h before the passage of the discontinuity. On the other hand, the interpretation of this feature as a scale-contracted cold front is also probable since it appeared to be closely linked (as revealed through synoptic analyses, surface pressure, and wind patterns) to the leading edge of a deep baroclinic zone that passed the station network between 1200 and 2400 UTC and that was marked by a 2000-km-long, 300-km-wide cloud band. It is also likely that the thunderstorms were triggered by the advancing cold front in the western part of the network and that the frontal structure was modified or masked by the thunderstorm outflows in a manner similar to that described by Seitter and Muench (1985). It would have been highly desirable to establish the exact placement of the frontal discontinuity within the deeper baroclinic system with the aid of adequately resolved horizontal wind observations in the immediate vicinity of the front during the crucial observation period. Unfortunately, the wind profiler was operating in the purely vertical mode and did not provide horizontal wind data. A recent study by Neiman et al. (1991) is more complete in this regard.

TABLE 1. Description of the various layers and zones in Fig. 14.

Zone	Primary characteristics	Vertical extent (km)
I	Postfrontal cold air, including the kinematic frontal boundary	0–1.4 (d_c = 1.4 km)
IIa	Prefrontal radiation inversion	0–0.3 (h_{INV} = 0.3 km)
IIb	Prefrontal air above the radiation inversion	0.3–3.0
IIc	Prefrontal air above the cold postfrontal air	1.0–3.0
III	A thin elevated isothermal layer or inversion	3.0–3.3 (d_{ISO} = 0.3 km)
IV	A neutral layer aloft	3.3–4.0 (d_N = 0.7 km)

Regardless of such limitations, there are several pointers to suggest that the atmospheric discontinuity probed by the Mesogers instrumental network had the distinct characteristics of a gravity current. Such pointers are 1) the suddenness of the wind shift; 2) the drop in temperature over a depth of approximately 1.4 km; 3) the rapid pressure rise of approximately 2 mb; 4) the narrow band of strong vertical velocities; and 5) a propagation speed close to what is calculated for a density or gravity current.

5. Gravity waves

a. *Overview*

Figure 14 is an idealized picture of the gravity current sensed by the Mesogers observational network ab-

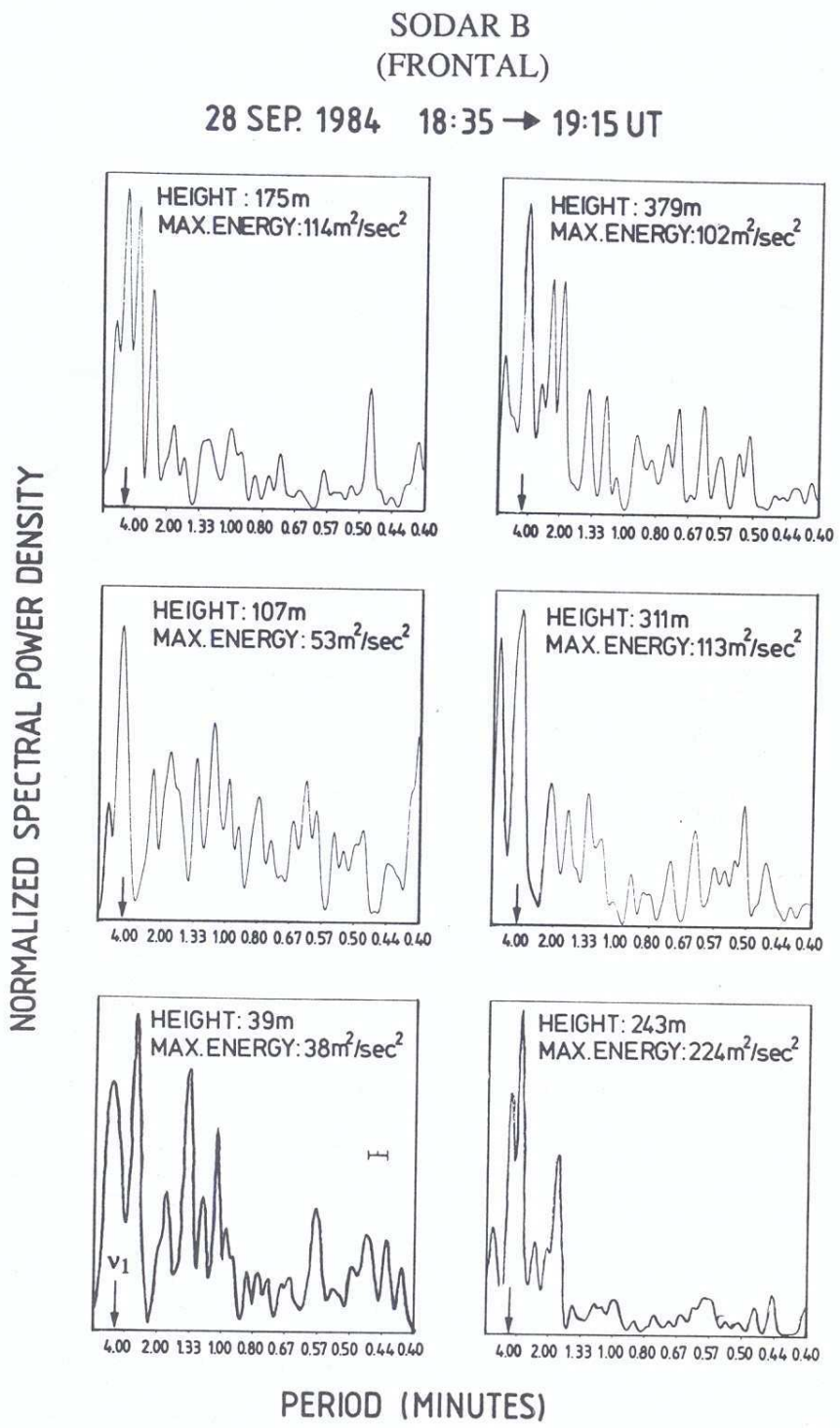

FIG. 15. Spectra of vertical velocities from sodar B at altitudes from 39 to 379 m AGL. Spectra are calculated using an FFT. Periods are labeled in minutes on the horizontal axis (same for each altitude), while the vertical axis is normalized to the maximum spectral power density at that altitude. The Nyquist period is 0.4 min. Spectra (a) before and during frontal passage (1835–1915 UTC), and (b) after frontal passage (1920–2000 UTC). The time intervals used for the spectra are marked in the facsimile chart from sodar B (Fig. 10b). Specific spectral peaks discussed in the text, ν_1 and ν_2, are marked with short and long arrows, respectively.

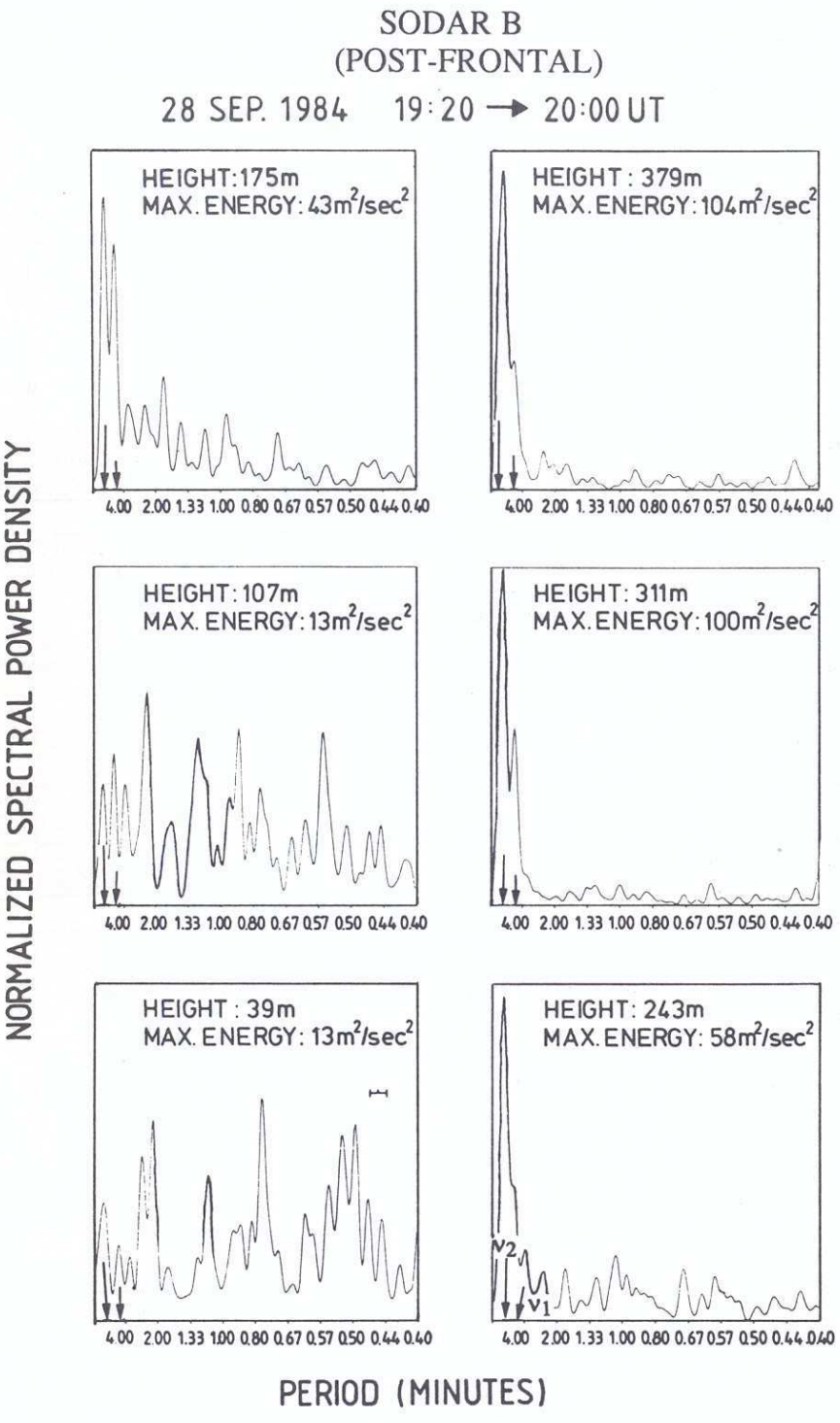

FIG. 15. (*Continued*)

stracted from the cross section in Fig. 9 containing the actual observations. The current is depicted as entering into a complex mesoscale environment characterized by zones and layers (Table 1), varying in their strength of stratification and location with respect to the gravity-current boundary. These ambient structures influence the incidence and vertical extent of gravity waves in a manner to be discussed in this section.

In order to quantify the apparent quasi-periodic behavior in both the wind profiler (Figs. 6 and 9) and

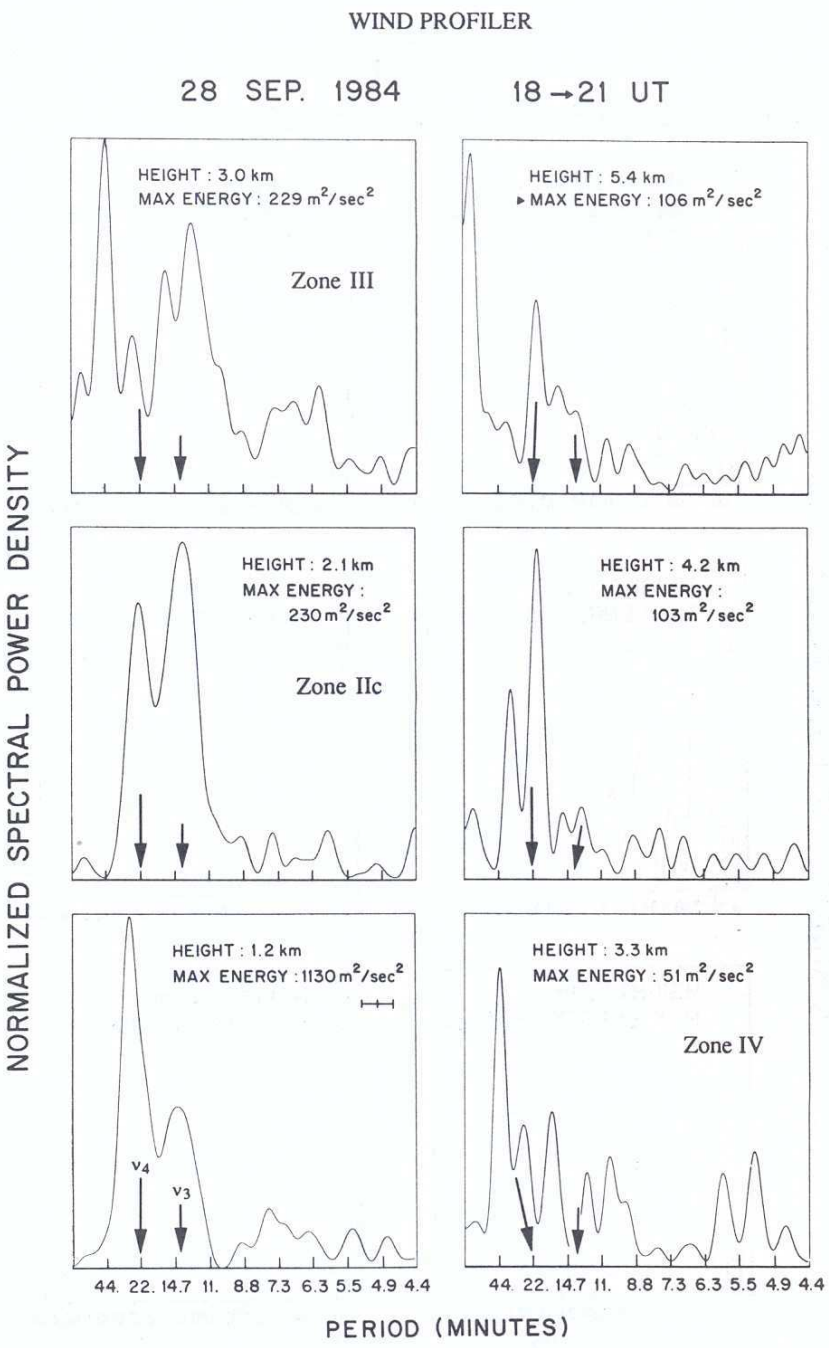

FIG. 16. Same as Fig. 15 except for spectra of radar-observed vertical velocities at selected altitudes from 1.2 to 5.4 km AGL from 1800 to 2100 UTC. The Nyquist period is 4.4 min. Specific spectral peaks ν_3 and ν_4 are marked with short and long arrows, respectively.

the sodar data (Fig. 10), a fast Fourier transform (FFT) routine has been employed to derive the vertical velocity spectra from these observations. These spectra are displayed in Figs. 15 and 16, respectively. The sodar spectra have been obtained for two separate 40-min time intervals in order to be able to detect differences in wave activity, if any, between the region ahead of and including the gravity-current front and the region in the colder air somewhat behind the front. The vertical scale for the spectral power density in each spec-

trum is linear and is normalized with respect to the maximum power density in that spectrum that has been indicated in order to facilitate comparisons between spectra for different times and altitudes. In addition, the half-power bandwidth of single frequencies is marked. A bandpass filter has been employed to produce time-amplitude plots of prominent waves of special interest in the spectra. Such plots are displayed in Figs. 17a,b and in Fig. 18. In studying these plots in detail, it should be kept in mind that the filtering process had a slight tendency to stretch the duration of the isolated waves.

b. *Wave description*

The description of gravity-wave activity in the gravity-current regime is now given on a zonewise basis where the zones are, as indicated in Fig. 14 and Table 1.

Starting with zone I, Figs. 10, 15, and 18 show that 1) the wave activity at the leading edge of the gravity current was more pronounced than in the cold air behind the discontinuity. 2) There were two prominent waves in this zone, one with a shorter period of approximately 5–5.5 min (ν_1) and the other with a longer period of 10–10.5 min (ν_2). 3) The shorter 5-min wave is evidently excited at the leading edge of the gravity current, and it extends horizontally about 10 km into the colder side of the front. This wave is strongest at approximately 250 m AGL, and it has little or no energy below approximately 60 m. This would suggest that the wave was either absorbed or reflected upward at or near the layer of strong postfrontal flow situated approximately 60 m AGL within the gravity current. 4) The longer 10-min wave is found in the cold air behind the front, where it has a horizontal extension of about 40 km. The vertical extent of the wave is, however, limited to above approximately 100 m, with an order of magnitude less wave energy at 100 m than at 175 m AGL.

There is sparser evidence for wave activity in zone IIa (i.e., in the prefrontal radiation inversion) as compared to zone I. Nonetheless, there appears to be a weak signal of a wavelike disturbance in the sodar A record (Fig. 10a). This disturbance feature is first observed approximately 30 min ahead of the gravity cur-

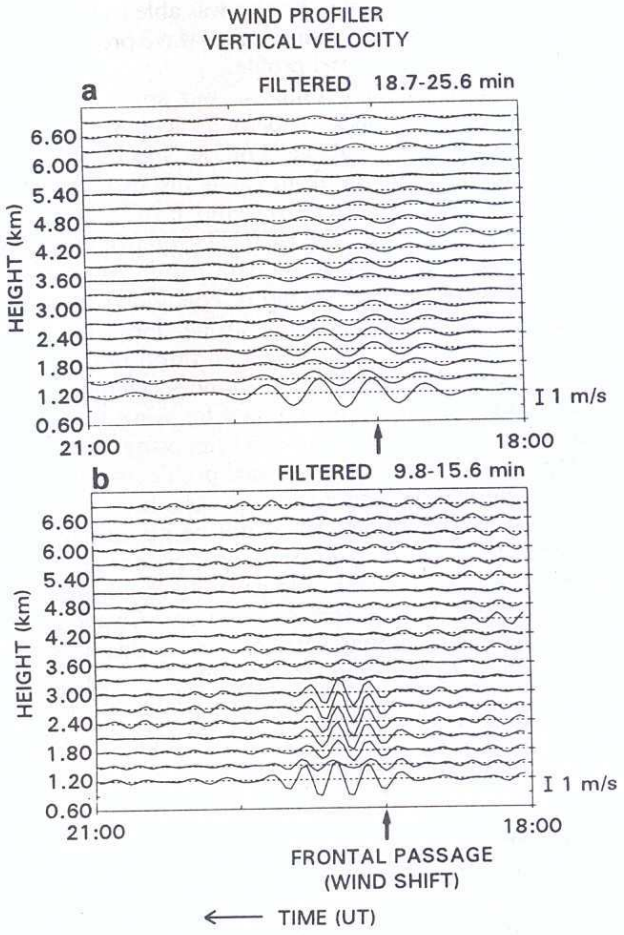

FIG. 17. Time series of bandpass-filtered vertical velocities observed by the 45-MHz wind profiler for the two dominant wave periods found in the spectra shown in Fig. 16: (a) 22 min, and (b) 14 min. The time of frontal passage at the wind-profiler site is also marked.

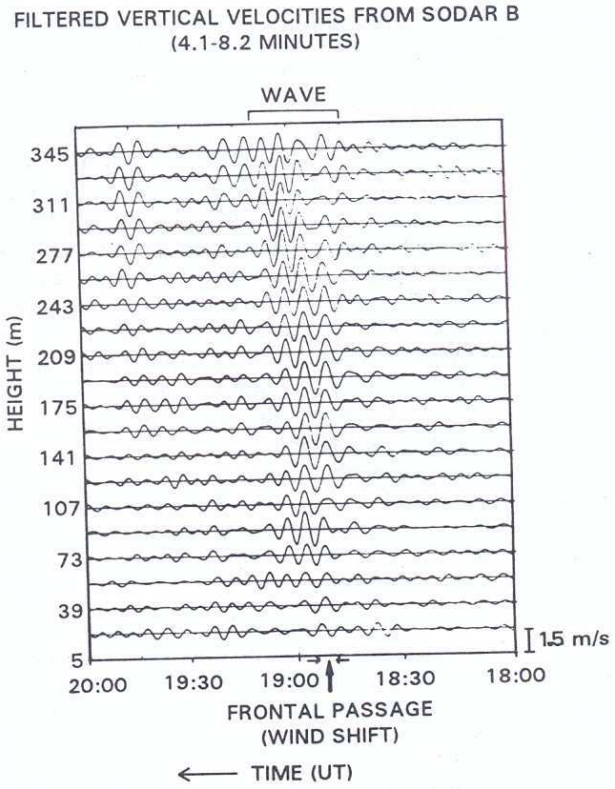

FIG. 18. Time series of bandpass-filtered vertical velocities at sodar B showing that the 5.5-min wave (spectral peak ν_1 in Fig. 15a) is localized at and behind the front. The filter retains waves with periods between 4.1 and 8.2 min. The front and its width are marked by arrows at the bottom.

rent front and lasts for approximately 15 min. It produces vertical displacements of 50–100 m. No similar disturbance is at once evident in the facsimile chart of sodar B (Fig. 10b), although the pocket of air found 1 min ahead of the front in the high-resolution data from that sodar (from 49 min 30 s to 50 min 15 s in Fig. 13b) shares the westerly flow of the postfrontal air, as if it were part of a borelike wave. As will be discussed in section 5d, the conditions were unfavorable for the formation of such waves in this case, a result that is consistent with the weak nature of the wavelike features seen in this zone.

The wind-profiler data in Fig. 6 contains no clear evidence of wave activity in zone IIb, although the filtered time series in Fig. 17a gives some indication of a 22-min wave ahead of the front. The presence of relatively long waves ahead of a front has been postulated previously (Ley and Peltier 1978), and the suggestion has been made that it might be involved in the scale-contraction process of cold fronts (Levy and Bretherton 1987; Gall et al. 1988).

The wave activity in zone IIc (i.e., in the prefrontal air that has been forced above the air behind the front) can be observed in Figs. 6 and 9. The commencement of this activity coincides almost exactly with frontal passage. It lasts for less than an hour and is mostly confined to altitudes below 3.5 km AGL. In the layer between 1.2 and 3.0 km AGL, two distinct waves are present with wave periods of 14 and 22 min, respectively. (The spectral peaks corresponding to these two waves are marked as ν_3 and ν_4 in Fig. 16.) Each of these waves is found to be strongest at the top of the cold air (i.e., at approximately 1.2 km) and weakest or nonexistent in the neutral layer (i.e., at 3.3 km). The 14-min wave is completely trapped by the neutral layer; notice the order of magnitude decrease in wave energy from below to above 3 km in Figs. 16 and 17b, as well as the absence of vertical tilt in the region where the wave is observed. In contrast, the 22-min wave still had substantial wave energy present at 4.2 km (Fig. 16), which is above the neutral layer, although there is a relative minimum of wave energy in the neutral layer for this longer wave as well.

The reader might notice from Fig. 17 that the perturbations at 1.5 and 1.8 km are somewhat damped and shifted relative to the perturbations above and below that layer. This behavior is also evident in the raw data (Fig. 6). It is uncertain whether this feature is real or is due to signal interference.

There is an additional spectral peak at a period of 44 min in the isothermal layer (Fig. 16). This feature is absent at other altitudes and, as such, may have to be considered somewhat as an anomaly.

Although zone IV (the neutral layer) is characterized by a relative minimum in wave activity, it has a decisive role to play in determining the vertical extent of waves associated with the gravity current. This will become clear in the next subsection.

c. Vertical wave propagation

Several features in our observations suggest that the vertical structure and propagation of gravity waves forced by the gravity current were under the control of ambient environmental factors such as thermal stratification and the wave-relative background wind profile. We have found that wave activity was more or less limited to altitudes below 3.5 km (Figs. 6 and 9); that the dominant waves in zone IIc (Fig. 14) had the structure of trapped waves with no vertical tilt (section 5b); and that some of the waves were stronger and lasted for several more wave periods than others.

Crook (1988) has used a numerical model to investigate specifically the influence of ambient wind and stratification on the gravity waves excited by a gravity current. He found that the waves were enhanced in the presence of a neutral layer aloft and that reflection of wave energy by an elevated inversion layer was maximized if the inversion had a thickness of one-fourth the vertical wavelength and was capped by a weakly stable layer of similar thickness. Making use of Scorer parameter profiles, he also was able to illustrate the crucial dependence of the vertical wave propagation on the wave-relative wind profile.

Application of such results to our study requires knowledge of wave phase velocity for which no direct measurements are available. For the special case of waves moving with the front (as is discussed in the next section), a wave-relative wind profile (Fig. 8) could be estimated from the 1850 UTC prefrontal wind sounding and from the sodar data behind the front. From this information it could be concluded that the trapping mechanism requiring strong opposing flow aloft was not likely to have been an important factor in this case since the wave-relative wind speed remained small aloft. An alternative method for wave trapping can occur when there is low-level opposing flow and strong curvature of the wind-speed profile above that. Such a feature was present in this case, but its effect on the Scorer parameter could not be quantified. In contrast, it is clear that the Scorer parameter approaches zero in the statically neutral layer from 3.3 to 4 km. The sudden decrease of observed wave amplitudes coincides closely with the base of this neutral layer (zone IV) and with the top of the isothermal layer (zone III). Hence, it appears certain that wave trapping above the front was aided by the neutral layer, although there may have been some possible contribution to trapping from the thin isothermal layer and/or from curvature in the wind-speed profile. The reduced stability in zones IIb and IIc was an additional factor that inhibited the vertical propagation of high-frequency waves at lower altitudes, either below the gravity-current front or in the prefrontal inversion.

Although wave energies at most frequencies were sharply reduced above the neutral layer, the longer period 22-min wave was apparently able to propagate

through it. The 800-m thickness of this layer must have presented more of a barrier to the shorter period waves than to the longer period waves.

Significant features of the ambient stratification such as the neutral layer (zone IV) and the inversion below it (zone III) are found to have appeared sometime between the 1400 UTC prefrontal and the 1923 UTC postfrontal soundings. It should be remarked that these characteristics of the stratification were not exceptional to our case alone. For example, very similar features were present in the case study of Mueller and Carbone (1987).

d. *Wave sources*

Discussion of the wave sources is hampered by the fact that our observations are restricted to wave periods without complementary information about either wavelengths or phase velocities. Nonetheless, it is still possible to use our observations to make consistency checks with theoretically predicted wave-forcing mechanisms.

1) KELVIN–HELMHOLTZ WAVES

The velocity shear and density difference required for the formation of KH waves are often present at the top of the cold-air pool in a gravity current, and such waves have been often detected in field observations and in laboratory studies or numerical models.

For the particular gravity current under study, the best estimates of the velocity shear across the cold-air interface, based on the prefrontal sounding (Fig. 8) and on sodar observations below 500 m, yield horizontal phase speeds for the KH waves of either 2.1 m s^{-1} toward 140° azimuth or 3.4 m s^{-1} toward 160° azimuth. These calculations are based on the Wegener hypothesis (Gossard and Hooke 1975) in which the direction is determined by the direction of the shear vector between the layers, while the speed is given by the projection of the layer mean onto that direction. The two phase velocity estimates are obtained depending on whether the wind profile directly above the cold air is the same as that observed at similar altitudes in the prefrontal sounding or if it more nearly corresponds to that of the prefrontal boundary-layer air that has been lifted up over the cold air. The possibility that the prefrontal air could have undergone lifting in this manner is suggested from the earlier comparison of the pre- and postfrontal soundings. This type of lifting is also evident in the observations of Mueller and Carbone (1987).

Using the phase speed c calculated for the velocity shear between zones I and IIc and the observed wave periods τ_{obs} in zone IIc, namely, 14 or 22 min, horizontal wavelengths λ_x can be calculated from the relationship $\lambda_x = c\tau_{obs}$. These estimates of λ_x are 1.8 or 2.8 km for c = 2.1 m s^{-1}, and 2.9 or 4.5 km for c = 3.4 m s^{-1}. Identifying λ_x as the fastest-growing wavelength, the linear theory of KH waves (Drazin 1958; Miles and Howard 1964) can now be applied to obtain a shear-layer thickness d_s between $\lambda_x/7.5$ and $\lambda_x/4.4$ or d_s = 0.3–0.7 km for τ_{obs} = 14 min, and d_s = 0.4–1.1 km for τ_{obs} = 22 min. The observed value for d_s of approximately 200–300 m, which is suggested by the thickness of the cold-air interface seen in the postfrontal sounding (Fig. 11) and which is reasonable for gravity currents in general (e.g., Mueller and Carbone 1987), is at the lower end of this range and corresponds more closely to the 14-min wave for which d_s = 0.3–0.7 km and $\lambda_x \sim$ 2–3 km. The activity of this wave was observed to be strongest at the cold-air interface, as would be the case if the wave had originated there. It is also of interest to note that the 14-min wave period is surprisingly close to the intrinsic buoyancy wave period (13 min) of the layer.

Shear-induced waves were observed not only at the top of the cold air but also in the postfrontal air near the surface (Fig. 10). Sodar wind profiles and the rawinsonde ascent at 1923 UTC showed significant velocity shear and low values for the Richardson number (<0.25) below 300 m AGL in the postfrontal air in zone I. The strength and thickness of the low-level postfrontal shear layer changed significantly with time, although its thickness never exceeded 300 m. This would indicate that the horizontal wavelengths of the shear-induced waves generated locally within the cold air would be short (<2 km). It is also likely that some of the waves observed in the postfrontal shear layer were originally formed on the cold-air interface yet had an impact at lower levels, a situation similar to that found in the example of Mueller and Carbone (1987).

2) SOLITARY WAVES AND INTERNAL BORES

If a gravity current enters a region containing a low-level stable layer, such as the prefrontal radiation inversion (zone IIa), internal bores or the closely related solitary waves may form. The conditions for the formation of these types of waves have been investigated in the laboratory by Rottman and Simpson (1989) and by numerical simulation by Haase and Smith (1989). Formation of these waves depends on the ratio of the depth of the prefrontal surface stable layer h_{INV} to the depth of the cold postfrontal air d_c. When the ratio $h_{INV}/d_c < 0.25$, Rottman and Simpson (1989) found in laboratory experiments that the prefrontal surface stable layer was readily mixed into the cold postfrontal air and that the gravity current was unaffected by its presence. This result has been confirmed in the numerical simulations of Haase and Smith (1989). In our study the ratio $h_{INV}/d_c \approx 0.2$, indicating that conditions for the formation of such waves were only marginal.

An additional consideration relating to the formation of undular waves ahead of the gravity-current front is whether the translation speed of the front C_{front} exceeds or falls short of the propagation speed C_0 of the waves

in the prefrontal stable layer. The propagation speed is given by $C_0 = 2NH/\pi$, where N is the buoyancy or Brunt–Väisälä frequency, and H is the depth of the stable layer (h_{INV} in this case). As reviewed in Rottman and Simpson (1989) and Haase and Smith (1989), if the front moves faster (slower) than the waves in the prefrontal inversion, a condition referred to as supercritical (subcritical), the resulting undulations will (will not) contain some postfrontal air. In our case, $C_0 = 5$ m s^{-1} (based on $T_{surface} = 19°C$, $T_{250\ m} = 25°C$, and $H = 250$ m) and $C_{front} = 10$ m s^{-1}. Hence, our case is supercritical, and any frontal undulations that may have formed would not have propagated ahead of the front (i.e., they would have contained postfrontal air). Thus, the disturbance noted ahead of the front in the facsimile chart from sodar A (Fig. 10a) most likely did not originate by this process. On the other hand, the very small feature noted at the front in Fig. 13 may have formed in this way since it was weak and was connected to the front.

3) Forced waves created by mechanical lifting of air at the front

In this section we hypothesize that the front acts as an obstacle over which the prefrontal air is forced upward and then downward behind the head of the gravity current, generating waves similar to lee waves (Gossard 1990). An analogous obstacle-like effect of convective elements in a sheared environment has been observed by Kuettner et al. (1987), and is suggested by Clark et al. (1986) to be a more efficient generator of gravity waves than even pure thermal forcing (penetrative convection).

Two specific conditions that need to be satisfied for the forcing of gravity waves by the gravity current in this manner are 1) the gravity current must have a well-defined head, as mentioned earlier, to force the waves in the first place; and 2) the air that is being forced upward must be stable. While the second condition is clearly met, the presence of a gravity-current head had to be inferred in our study since, with the exception of a single rawinsonde ascent, we were unable to observe the upper boundary of the gravity current. The observed existence of a neutral layer aloft, however, should have aided in maintaining such waves, once excited, at fairly large amplitudes by not allowing substantial wave energy to leak through to higher levels.

The period of the wave forced by the gravity current can be estimated as follows. Based on the average prefrontal airspeed of 6 m s^{-1}, which is antiparallel to the gravity current, and the propagation speed of 10 m s^{-1} for the gravity current itself, the front-relative velocity of air parcels within the wave is approximately 16 m s^{-1}. The wavelength λ of the wave is the distance traveled by such air parcels in one buoyancy period, which is observed to be 13 min. The wavelength is therefore $\lambda = 12.5$ km. On the assumption that the waves are stationary in the moving reference frame of the gravity current, the phase velocity C of the wave can be equated to the propagation velocity of the current (10 m s^{-1}). This gives the wave period $\tau = (\lambda/c) = 21$ min, which is in close agreement with the 22-min period observed in the radar vertical velocity spectra (Fig. 16). Notice also that the deduced wavelength of 12.5 km is such that the wave would have propagated through the weakly stable layer between 2 and 3 km but would have become evanescent in the neutral layer from 3.2 to 4 km AGL (Fig. 14).

6. Summary

The case study of a gravity current reported in this paper serves to illustrate the potential usefulness of remote-sensing instruments like the sodar and the radar wind profiler in revealing 1) the detailed structure of such currents, 2) the structure and mode of excitation of waves forced by such currents, and 3) the influence of ambient stratification on the wave fields. Our particular study could have benefited from the horizontal wind information and better height coverage that are typically available from wind profilers as they now exist. Such observations would have provided a more complete picture of the gravity current than was possible in this study because of the vertical gap between the radar and sodar data. More detailed information about the thermal structure of the environment would also have been desirable, as can now be obtained by employing the radio acoustic sounding system technique. With such better coordination of available techniques, it should be possible to investigate the generation of gravity currents and their two-way interaction with their mesoscale environment in a more thorough fashion.

Acknowledgments. Valuable assistance from Fabrice Cuq and early efforts of H. J. Kim are gratefully acknowledged. We have benefited from the detailed and constructive criticism of M. Shapiro, R. Wakimoto, and an anonymous referee, as well as from several helpful comments from P. Neiman and T. Weckwerth. This work has been supported under National Science Foundation Grant ATM84-19371. The Mesogers experiment was supported by Institut des Sciences de l'Univers Contracts 4647 and 4687.

REFERENCES

Carbone, R. E., 1982: A severe frontal rainband. Part I: Stormwide hydrodynamic structure. *J. Atmos. Sci.*, **39**, 258–279.

——, J. W. Conway, N. A. Crook, and M. W. Moncrieff, 1990: The generation and propagation of a nocturnal squall line. Part I: Observations and implications for mesoscale predictability. *Mon. Wea. Rev.*, **118**, 26–49.

Cheung, T. K., and C. G. Little, 1990: Meteorological tower, microbarograph array, and sodar observations of solitary-like waves in the nocturnal boundary layer. *J. Atmos. Sci.*, **47**, 2516–2536.

Clark, T. L., T. Hauf, and J. P. Kuettner, 1986: Convectively forced internal gravity waves: Results from two-dimensional numerical experiments. *Quart. J. Roy. Meteor. Soc.*, **112**, 899–925.

Crook, N. A., 1988: Trapping of low-level internal gravity waves. *J. Atmos. Sci.*, **45,** 1533–1541.

Doviak, R. J., S. S. Chen, and D. R. Christie, 1991: A thunderstorm-generated solitary wave observation compared with theory for nonlinear waves in a sheared atmosphere. *J. Atmos. Sci.*, **48,** 87–111.

Drazin, P. G., 1958: The stability of a shear layer in an unbounded heterogeneous inviscid fluid. *J. Fluid Mech.*, **4,** 214–224.

Droegemeier, K. K., and R. B. Wilhelmson, 1987: Numerical simulation of thunderstorm outflow dynamics: Part I: Outflow sensitivity experiments and turbulence dynamics. *J. Atmos. Sci.*, **44,** 1180–1210.

Fulton, R., D. S. Zrnic, and R. J. Doviak, 1990: Initiation of a solitary wave family in the demise of a nocturnal thunderstorm density current. *J. Atmos. Sci.*, **47,** 319–337.

Gage, K. S., 1990: Radar observations of the free atmosphere: Structure and dynamics. *Radar in Meteorology,* D. Atlas, Ed., Amer. Meteor. Soc., 534–565.

Gall, R. L., R. T. Williams, and T. L. Clark, 1988: Gravity waves generated during frontogenesis. *J. Atmos. Sci.*, **45,** 2204–2219.

Goff, R. C., 1976: Vertical structure of thunderstorm outflows. *Mon. Wea. Rev.*, **104,** 1429–1440.

Gossard, E. E., 1990: Radar research in the atmospheric boundary layer. *Radar in Meteorology,* D. Atlas, Ed., Amer. Meteor. Soc., 477–527.

——, and W. H. Hooke, 1975: *Waves in the Atmosphere.* Elsevier, 456 pp.

Haase, S. P., 1991: Numerical simulation of the bore-like cold front of 8 October 1987 in southern Germany. *Tellus,* **43A,** 97–105.

——, and R. K. Smith, 1989: The numerical simulation of atmospheric gravity currents. Part II: Environments with stable layers. *Geophys. Astrophys. Fluid Dyn.*, **46,** 35–51.

Hoinka, K. P., M. Hagen, H. Volkert, and D. Heimann, 1990: On the influence of the Alps on a cold front. *Tellus,* **42A,** 140–164.

Koch, S. E., P. B. Dorian, R. Ferrare, S. H. Melfi, W. C. Skillman, and D. Whiteman, 1991: Structure of an internal bore and dissipating gravity current as revealed by Raman lidar. *Mon. Wea. Rev.*, **119,** 857–887.

Kuettner, J. P., P. A. Hildebrand, and T. L. Clark, 1987: Convection waves: Observations of gravity wave systems over convectively active boundary layers. *Quart. J. Roy. Meteor. Soc.*, **113,** 445–467.

Levy, G., and C. S. Bretherton, 1987: On a theory of the evolution of surface cold fronts. *J. Atmos. Sci.*, **44,** 3413–3418.

Ley, B. E., and W. R. Peltier, 1978: Wave generation and frontal collapse. *J. Atmos. Sci.*, **35,** 3–17.

Mahoney, W. P., 1988: Gust front characteristics and the kinematics associated with interacting thunderstorm outflows. *Mon. Wea. Rev.*, **116,** 1474–1491.

Miles, J. W., and L. N. Howard, 1964: Note on a heterogeneous shear flow. *J. Fluid Mech.*, **20,** 331–336.

Mueller, C. K., and R. E. Carbone, 1987: Dynamics of a thunderstorm outflow. *J. Atmos. Sci.*, **44,** 1881–1898.

Nastrom, G. D., M. R. Peterson, J. L. Green, K. S. Gage, and T. E. VanZandt, 1990: Sources of gravity wave activity seen in the vertical velocities observed by the Flatland VHF radar. *J. Appl. Meteor.*, **29,** 783–792.

Neiman, P. J., B. B. Stankov, P. T. May, and M. A. Shapiro, 1991: Radio acoustic sounding system observations of an arctic front. *J. Appl. Meteor.*, **30,** 1646–1651.

Orlanski, I., 1975: A rational subdivision of scales for atmospheric processes. *Bull. Amer. Meteor. Soc.*, **56,** 527–530.

Parsons, D. B., M. A. Shapiro, R. M. Hardesty, R. J. Zamora, and J. M. Intrieri, 1991: The finescale structure of a West Texas dryline. *Mon. Wea. Rev.*, **119,** 1242–1258.

Rottman, J. W., and J. E. Simpson, 1989: The formation of internal bores in the atmosphere: A laboratory model. *Quart. J. Roy. Meteor. Soc.*, **115,** 941–963.

Seitter, K. L., 1986: A numerical study of atmospheric density current motion including the effects of condensation. *J. Atmos. Sci.*, **43,** 3068–3076.

——, and H. S. Muench, 1985: Observation of a cold front with rope cloud. *Mon. Wea. Rev.*, **113,** 840–848.

Shapiro, M. A., 1984: Meteorological tower measurements of a surface cold front. *Mon. Wea. Rev.*, **112,** 1634–1639.

——, T. Hampel, D. Rotzoll, and F. Mosher, 1985: The frontal hydraulic head: A micro-α scale (1 km) triggering mechanisms for mesoconvective weather systems. *Mon. Wea. Rev.*, **113,** 1166–1183.

Simpson, J. E., 1987: *Gravity Currents in the Environment and the Laboratory.* John Wiley & Sons, 244 pp.

——, and R. E. Britter, 1980: A laboratory model of an atmospheric mesofront. *Quart. J. Roy. Meteor. Soc.*, **106,** 485–500.

——, D. S. Mansfield, and J. R. Milford, 1977: Inland penetration of sea-breeze fronts. *Quart. J. Roy. Meteor. Soc.*, **103,** 47–76.

Smith, R. K., and M. J. Reeder, 1988: On the movement and low-level structure of cold fronts. *Mon. Wea. Rev.*, **116,** 1927–1944.

Stull, R. B., 1976: Internal gravity waves generated by penetrative convection. *J. Atmos. Sci.*, **33,** 1279–1286.

Wakimoto, R. M., 1982: The life cycle of thunderstorm gust fronts as viewed with Doppler radar and rawinsonde data. *Mon. Wea. Rev.*, **110,** 1060–1082.

Weckwerth, T. M., and R. M. Wakimoto, 1991: Convection initiation associated with a gust front and Kelvin–Helmholtz instability. Preprints, *25th Conf. on Radar Meteorology,* Paris, Amer. Meteor. Soc., 454–457.

Weill, A., C. Mazaudier, F. Baudin, C. Klapisz, F. Leca, M. Masmoudi, D. Vidal Madjar, R. Bernard, O. Taconet, B. S. Gera, A. Sauvaget, A. Druilhet, P. Durand, J. Y. Caneil, P. Mery, G. Dubosclard, A. C. M. Beljaars, W. A. A. Monna, J. G. Van Der Vliet, M. Crochet, D. Thomson, and T. Carlson, 1988: The "Mesogers 84" experiment: A report. *Bound.-Layer Meteor.*, **42,** 251–264.

Young, G. S., and R. H. Johnson, 1984: Meso- and microscale features of a Colorado cold front. *J. Climate Appl. Meteor.*, **23,** 1315–1325.